

## THE GAS ENVIRONMENT OF THE YOUNG STELLAR OBJECT GL 2591 STUDIED BY INFRARED SPECTROSCOPY

GEORGE F. MITCHELL<sup>1</sup> AND CHARLES CURRY  
 Saint Mary's University, Halifax

JEAN-PIERRE MAILLARD<sup>1</sup>  
 Institut d'Astrophysique, Paris

AND

MARK ALLEN<sup>1</sup>

Jet Propulsion Laboratory, Pasadena

Received 1988 September 16; accepted 1988 November 15

### ABSTRACT

We present and discuss a high-resolution ( $0.0569 \text{ cm}^{-1}$ )  $M$  band ( $4.6 \mu\text{m}$ ) spectrum of the deeply embedded young stellar object GL 2591. The spectrum shows (a) strong  $^{12}\text{CO}$  ( $v = 0-1$ ) absorption lines with the very large velocity width of greater than or equal to  $130 \text{ km s}^{-1}$ ; (b)  $^{13}\text{CO}$  ( $v = 0-1$ ) absorption lines with rotational quantum numbers up to  $J = 23$ , at the velocity of the molecular cloud core; (c)  $^{13}\text{CO}$  ( $v = 0-1$ ) absorption lines due to gas receding from GL 2591 at  $\sim 17 \text{ km s}^{-1}$ ; (d) the first detection in a young stellar object of absorption lines due to vibrationally excited  $^{12}\text{CO}$ .

Analysis of the data shows a variety of physical structures with a wide range of gas properties. (1) A discrete absorption feature is seen which has an outflow velocity of  $\sim 17 \text{ km s}^{-1}$  and a temperature of 200 K. The 200 K gas, if heated by collisions with warm grains, can be interpreted as a fragment or shell at a distance of  $\sim 1000 \text{ AU}$  from the central object and recently ( $\leq 250 \text{ yr}$ ) ejected. (2) We find cold gas with  $T = 38 \text{ K}$  which we identify with the core of the molecular cloud within which GL 2591 is embedded. (3) The high  $J$  lines of  $^{13}\text{CO}$ , at the same velocity as the cold gas, imply hot ( $T \approx 1000 \text{ K}$ ) dense ( $n \geq 10^7 \text{ cm}^{-3}$ ) gas. The existence of a significant population ( $\sim 1\%$ ) of vibrationally excited CO in the hot gas implies even higher densities,  $n \geq 10^{10} \text{ cm}^{-3}$ , for this gas. The 1000 K gas, if heated by gas-grain collisions, is a shell or disk within several tens of AU of the central object. (4) The very broad  $^{12}\text{CO}$  lines are formed in a neutral wind which probably possesses a temperature gradient and contains gas with temperatures as high as 500 K.

The hot, low-velocity gas together with the warm, high velocity gas suggest, but do not compel, a physical picture in which a warm neutral wind accelerates from an accretion disk.

*Subject headings:* infrared: sources — infrared: spectra — stars: individual (GL 2591) — stars: pre-main-sequence

### I. INTRODUCTION

GL 2591 is a luminous infrared source with many of the properties generally thought to characterize protostars or young stellar objects. It is deeply embedded in molecular gas, with a visual extinction of about 50 mag (Lada *et al.* 1984). If the distance to GL 2591 is 1 kpc, as quoted by Mozurkewich, Schwartz, and Smith (1986), its luminosity is  $\sim 2 \times 10^4 L_{\odot}$ . The near-infrared emission, shortward of  $\sim 13 \mu\text{m}$ , is well explained by a compact (angular size  $\approx 0''.06$ ) dust shell with a temperature of  $\sim 800 \text{ K}$  (Lada *et al.* 1984). GL 2591 is the center of an extended high-velocity molecular outflow of a bipolar nature: CO emission-line wings extend over about  $40 \text{ km s}^{-1}$  (Bally and Lada 1983). In spite of the fairly large dynamical age indicated by the extended outflow ( $\sim 3 \times 10^4 \text{ yr}$  if the distance is 1 kpc), no ionized gas is detected at the position of the infrared source (Thompson and Tokunaga 1979; Campbell 1984). Near-infrared images of GL 2591 (Forrest and Shure 1986) show an arc or loop to one side of the young stellar object. The loop is interpreted as the outline of a cavity

of dimension  $\sim 10^4 \text{ AU}$ . A map in the CS molecule (Yamashita *et al.* 1987) shows a flattened structure oriented perpendicular to the axis of the CO outflow.

Infrared absorption spectroscopy of GL 2591 has demonstrated that lines of the fundamental vibrational band of CO are unusually strong and broad. The CO lines were detected easily by Lacy *et al.* (1984) using an instrument with a velocity resolution of  $\sim 350 \text{ km s}^{-1}$ . Geballe and Wade (1985) observed two lines of the fundamental band of CO with a resolution of  $\sim 12 \text{ km s}^{-1}$  and found the lines to have a total width of  $\sim 100 \text{ km s}^{-1}$  and the CO to be hot ( $T_{\text{ex}} \approx 1000 \text{ K}$ ). They interpreted the high-velocity gas as a neutral outflow very close to the central object. The presence of a neutral outflow (or wind) from GL 2591 has important implications for the energetics of this source as well as for the nature of the outflow mechanism in general. The observations of Geballe and Wade were limited to only two lines (the R2 and P26 lines) of the CO band. Furthermore, the Doppler shift of GL 2591 at the time of their observations was such that the telluric CO R2 line partially obscured the R2 line in the source. The desirability of obtaining improved physical properties for the gas near GL 2591 motivated us to obtain a high-resolution infrared spectrum of this source using a Fourier transform spectrometer (FTS) with broad wavelength coverage.

<sup>1</sup> Visiting Astronomer, Canada-France-Hawaii telescope, operated by the National Research Council of Canada, the Centre National de la Recherche Scientifique of France, and the University of Hawaii.

## II. OBSERVED CO FEATURES

The observations presented here were taken using the Fourier transform spectrometer at the Cassegrain focus of the Canada-France-Hawaii telescope on Mauna Kea, Hawaii, on the night of 1987 July 9–10. Details of the FTS can be found in Maillard and Michel (1982). We employed a filter with a pass-band from  $2080$  to  $2180$   $\text{cm}^{-1}$  ( $4.59$   $\mu\text{m}$  to  $4.81$   $\mu\text{m}$ ). A spectral resolution of  $0.0569$   $\text{cm}^{-1}$  was used, corresponding, at  $4.7$   $\mu\text{m}$ , to  $\lambda/\Delta\lambda = 37,000$  and a velocity resolution of  $8.0$   $\text{km s}^{-1}$ . To limit the thermal background, we used a small aperture of  $2''.5$ . The total integration time was 80 minutes, over a range of airmass from 1.1 to 1.3. Correction for absorption lines in Earth's atmosphere was accomplished by the observation of a standard star,  $\alpha$  Lyr. The spectrum of  $\alpha$  Lyr was taken on the same night with an integration time of 64 minutes over a range of airmass from 1.2 to 1.4. The  $2\sigma$  signal-to-noise ratio of the GL 2591 spectrum is 45; that of the  $\alpha$  Lyr spectrum is 36.

The fundamental absorption band is formed when CO molecules in the ground vibrational state ( $v = 0$ ) are raised to the first excited vibrational state ( $v = 1$ ) by the absorption of infrared ( $\sim 4.6$   $\mu\text{m}$ ) photons. If the initial rotational state is  $J$ , the selection rule  $\Delta J = \pm 1$  ensures that the final rotational state is  $J \pm 1$ . The transitions  $(0, J)$  to  $(1, J + 1)$  constitute the  $R$  branch; transitions  $(0, J)$  to  $(1, J - 1)$  comprise the  $P$  branch. In the spectrum of GL 2591 we see series of absorption features due to  $^{12}\text{CO}$  and  $^{13}\text{CO}$ .

The spectrum of GL 2591 is shown in compressed form in Figure 1. No correction has been made in Figure 1 for telluric absorption or for the shape of the bandpass. Figure 2a–d shows the spectrum GL 2591 (above) and the spectrum of  $\alpha$  Lyr (below). Extremely strong and broad lines of the fundamental vibrational band ( $v = 0-1$ ) of  $^{12}\text{C}^{16}\text{O}$  are immediately apparent in Figure 2. The GL 2591 CO lines are Doppler-shifted by  $-32$   $\text{km s}^{-1}$ , well clear of the telluric lines. A portion of the spectrum near the  $P3$  ( $J = 3-2$ ) line of  $^{12}\text{CO}$  is shown in Figure 3, where the GL 2591 and Vega spectra are superposed to show the low noise of both. The ratio spectrum, GL 2591 divided by  $\alpha$  Lyr, is shown in Figure 4.

We have obtained average line profiles using the lines which are free of strong telluric features. These are shown in Figure 5. Because the low  $J$  lines of the strongest  $^{13}\text{CO}$  velocity component are formed in cold gas and the high  $J$  lines are formed in hot gas (see § III below), we display in Figure 5 average  $^{13}\text{CO}$  profiles for low  $J$  and high  $J$  lines separately. Three-velocity components show clearly in the  $^{12}\text{CO}$  and  $^{13}\text{CO}$  fundamental band profiles (Fig. 5a, b, and c). The average profile of the vibrationally excited  $^{12}\text{CO}$  feature shows only a single component at the velocity of the strongest fundamental band component.

### a) Broad Velocity $^{12}\text{CO}$ ( $v = 0-1$ )

Very strong and broad absorption lines of the fundamental band of  $^{12}\text{CO}$  are prominent in Figures 2, 4, and 5a. The transitions from  $P15$  to  $R9$  are present in the spectrum, each extending over the wide velocity range  $v_{\text{LSR}} \approx 0$  to  $-130$   $\text{km s}^{-1}$ . The lines are markedly asymmetrical, with an extended blue wing. The  $^{12}\text{CO}$  profiles in Figure 4 and the composite profile in Figure 5a show two fairly well-separated absorption minima as well as a third absorption component to the blue which is blended with the middle component. The blue wing of the  $^{12}\text{CO}$   $v = 0-1$  lines shows some structure and may consist, in whole or in part, of unresolved lines. As we will discuss below, the three strongest features of the  $^{12}\text{CO}$  line have counterparts in  $^{13}\text{CO}$ . Analysis of the  $^{13}\text{CO}$  lines and the unsaturated blue wings of the  $^{12}\text{CO}$  lines (§ III below) shows that the gas temperature of the high-velocity gas is different from that of the two strongest components. It appears, therefore, that the observed  $^{12}\text{CO}$  profile consists of saturated components superposed on a broad, high-velocity absorption feature.

### b) $^{13}\text{CO}$ Absorption Features at $v_{\text{LSR}} = -11$ $\text{km s}^{-1}$ , $-28$ $\text{km s}^{-1}$ , and $-38$ $\text{km s}^{-1}$

Our filter bandpass includes a portion of the fundamental band of  $^{13}\text{CO}$ , from the  $P4$  transition to the  $R23$  transition. The  $^{13}\text{CO}$  lines are labeled in Figure 4 below the spectrum.

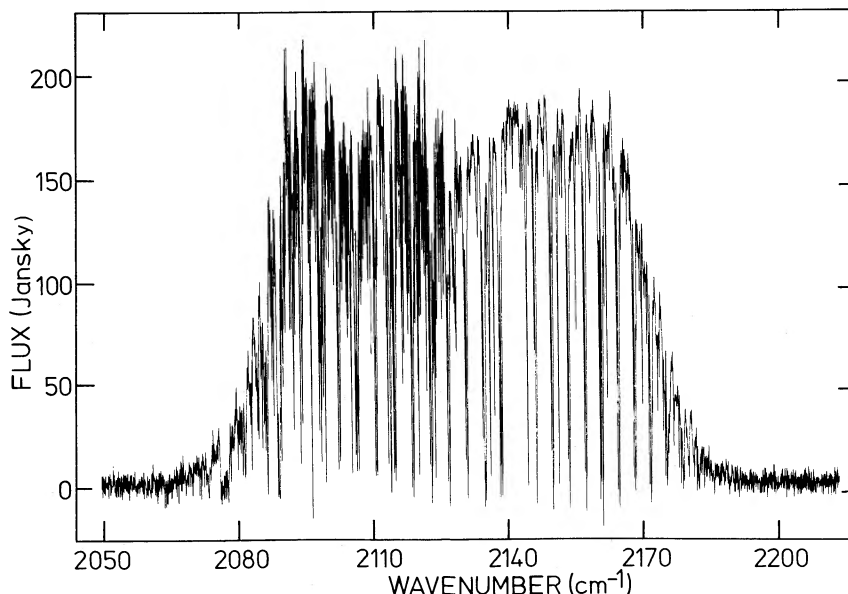


FIG. 1.—The complete spectrum of GL 2591 is shown to illustrate the bandpass of the filter. The spectrum is unapodized and uncorrected for telluric absorption.

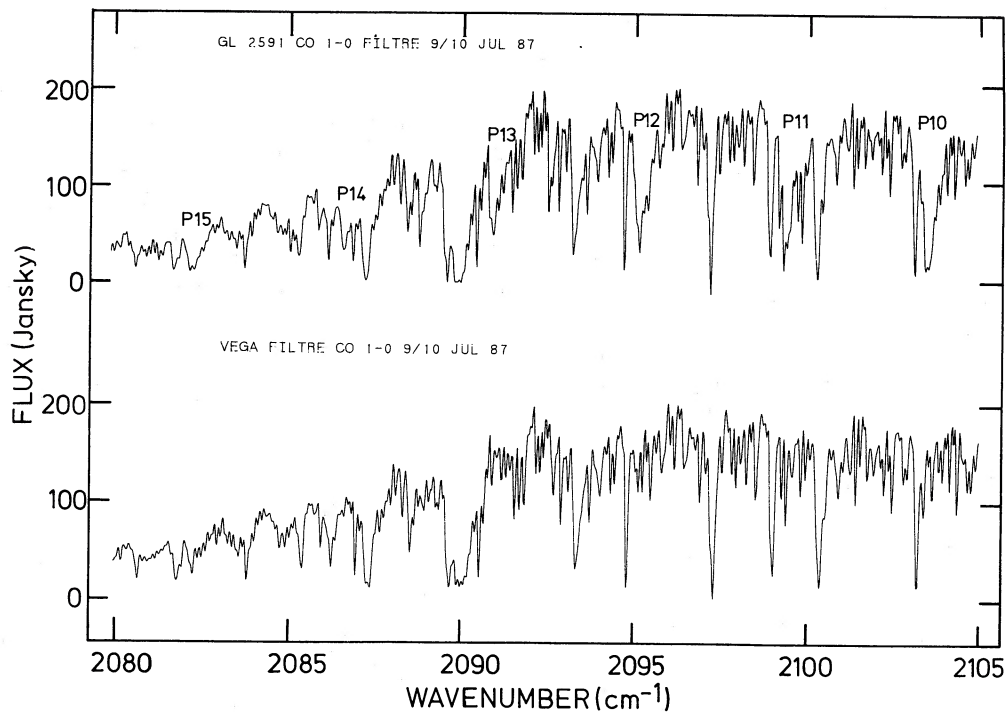


FIG. 2a

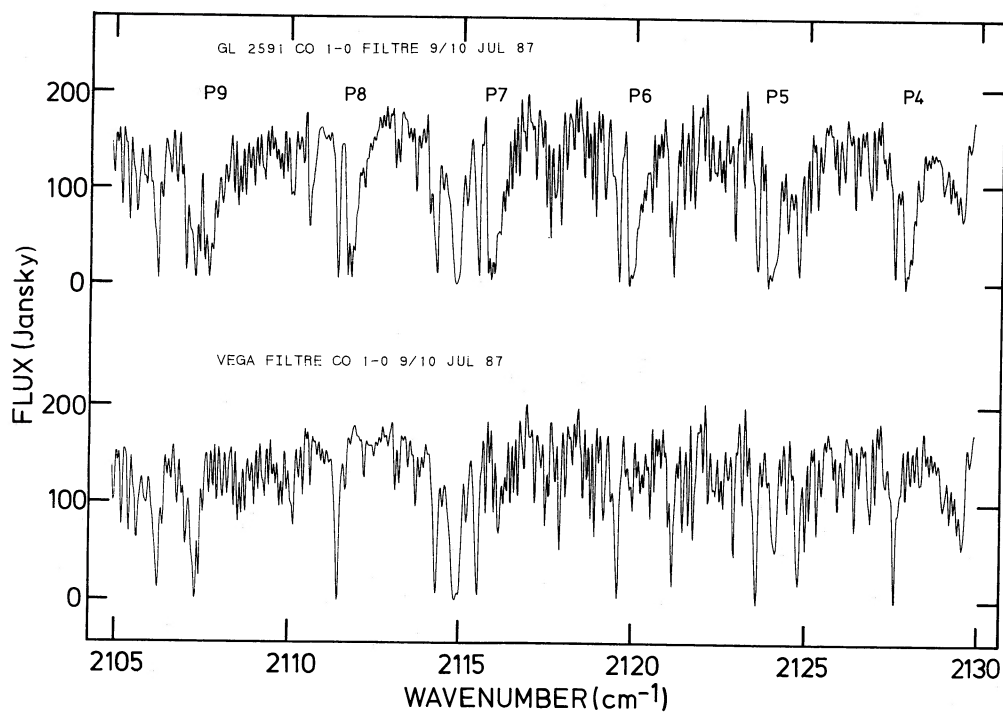


FIG. 2b

FIG. 2.—The spectrum of GL 2591 is shown on the top and the spectrum of a reference star,  $\alpha$  Lyr, is shown below. The strong and broad absorption lines of  $^{12}\text{CO}$  ( $v = 0-1$ ) are labeled (P15 to R9).

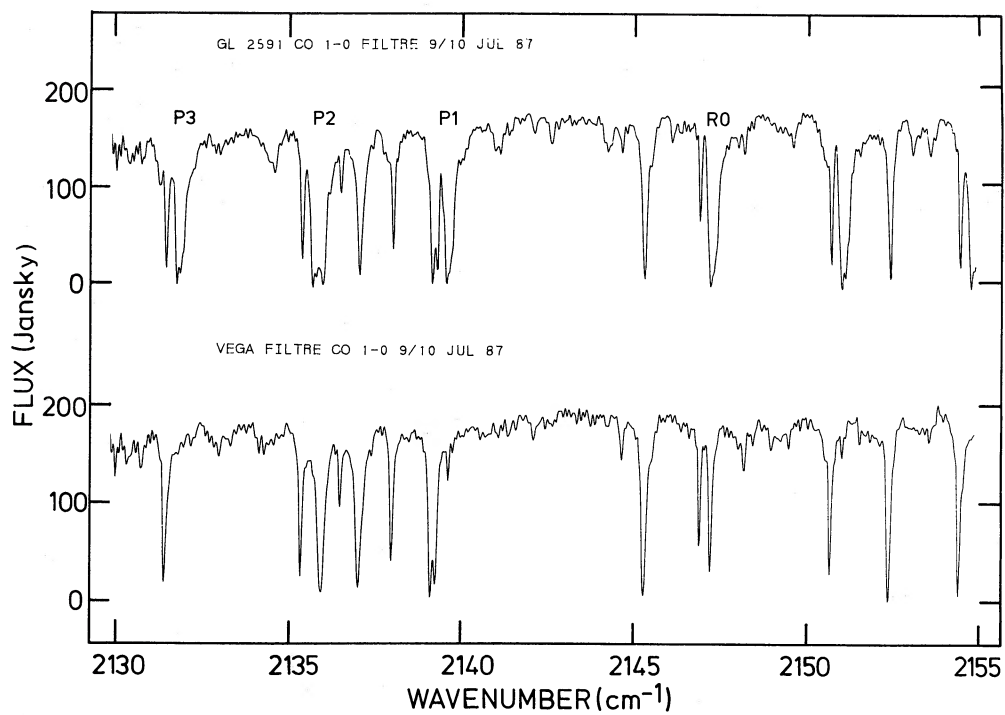


FIG. 2c

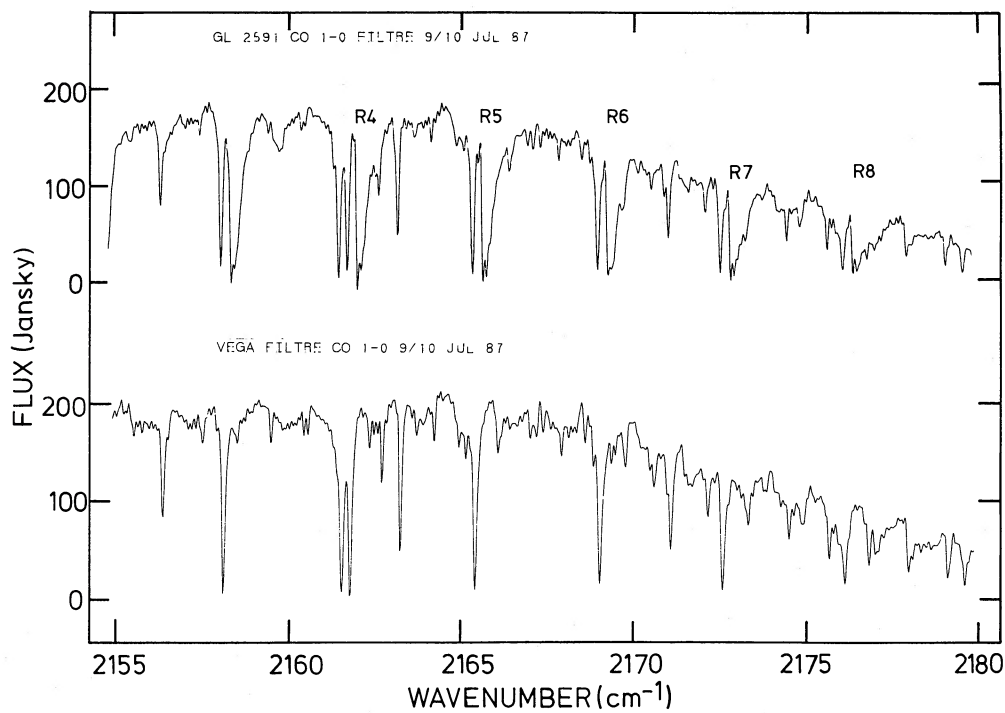


FIG. 2d

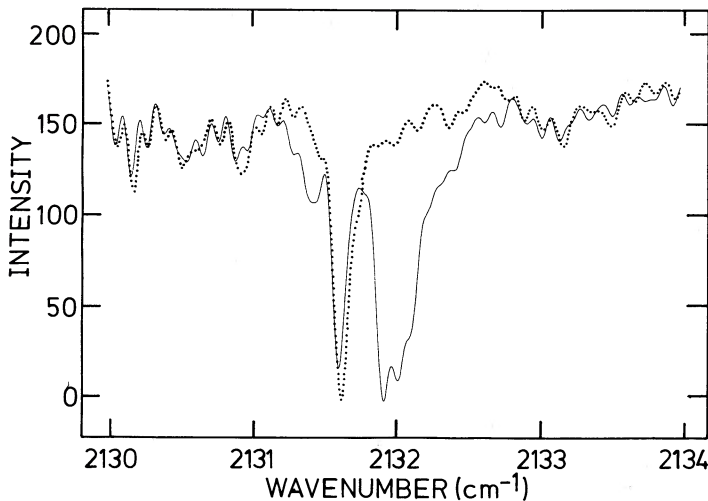


FIG. 3.—A portion of the spectrum centred on the  $P3$  ( $J=3-2$ ) line of  $^{12}\text{CO}$  illustrates the structure of the  $^{12}\text{CO}$  absorption lines. The spectrum of  $\alpha$  Lyr is shown by a dotted line.

The  $^{13}\text{CO}$  lines show the same three components as do the  $^{12}\text{CO}$  lines, but there is no broad  $^{13}\text{CO}$  absorption corresponding to the  $^{12}\text{CO}$  blue wing. The two strongest  $^{13}\text{CO}$  velocity components are well separated in the low  $J$  lines (Fig. 5b), but are blended in the higher  $J$  lines (Fig. 5c). The bluest velocity component is blended with the central component for all  $^{13}\text{CO}$  lines. It is evident from Figures 4 and 5 that in the low-velocity component the  $^{13}\text{CO}$  lines with lower rotational quantum numbers are much stronger than the higher  $J$  lines. Analysis of the feature (discussed in § III below) shows that the low  $J$  lines are formed in cold gas whereas the higher  $J$  lines are formed in hot gas. Because we cannot assume that the cold and hot gas have a common velocity, we have obtained a mean LSR velocity for the high  $J$  and low transitions separately. We find  $v_{\text{LSR}} = -10.7 \pm 0.4 \text{ km s}^{-1}$  for lines with  $J \leq 6$  and  $v_{\text{LSR}} = -8 \pm 5 \text{ km s}^{-1}$  for lines with  $J \geq 9$ . Here, and subsequently,  $1 \sigma$  uncertainties, reflecting the scatter in the measured line positions, are quoted. The scatter is larger for the weaker high  $J$  lines. The high  $J$  and low  $J$  velocities agree to within  $1 \sigma$ : we adopt a  $v_{\text{LSR}}$  of  $-11 \text{ km s}^{-1}$  for the feature.

The central  $^{13}\text{CO}$  absorption feature can be reliably detected in transitions out to R16. Its mean LSR velocity is  $-28 \pm 3 \text{ km s}^{-1}$ . The third component has a mean LSR velocity of  $\sim -38 \text{ km s}^{-1}$ .

### c) *Vibrationally Excited* $^{12}\text{CO}$ ( $v=1-2$ )

A series of 10 absorption lines from  $^{12}\text{CO}$  in the first excited vibrational state are present in the spectrum (namely, the P8, P6, P5, P4, R5, R6, R7, R8, R9, and R12 lines). To our knowledge, GL 2591 is the first young stellar object in whose spectrum absorption lines from vibrationally excited CO have been seen. The lines are labeled in Figure 4 by the notation P8\*, R6\*, etc. The mean velocity of the excited CO lines,  $v_{\text{LSR}} = -9 \pm 2 \text{ km s}^{-1}$ , is essentially identical to the velocity of the “ $-11 \text{ km s}^{-1}$ ”  $^{13}\text{CO}$  feature. Although the  $v=1-2$  lines are individually fairly weak, the presence of 10 lines of the series makes the identification secure. All the  $v=1-2$  lines which fall in clear portions of the bandpass are detected. The several lines which are missing fall on other absorption features.

### III. PHYSICAL PROPERTIES OF THE ABSORBING GAS

Equivalent widths of the CO lines are measured from the ratio spectrum, GL 2591 divided by  $\alpha$  Lyr. The velocity component at  $-38 \text{ km s}^{-1}$  is so badly blended that we have not measured equivalent widths for this component. Because the FTS spectra are subject to channeling, a sinusoidal modulation of the intensity, care must be taken in matching the continuum of the source and the standard in the neighborhood of each line before a ratio is taken. For an optically thin line, the column density of CO in the initial rotational state of the transition,  $N_J$ , can be found directly from the equivalent width using the relation  $W_\omega = (\pi e^2/m_e c^2) f_J N_J$ , where  $W_\omega$  is the equivalent width,  $f_J$  is the absorption oscillator strength of the transition (from Kirby-Docken and Liu 1978), and the other symbols have their usual meaning.

If the carbon monoxide energy levels are populated according to thermodynamic equilibrium, the Boltzmann equation applies, and so  $N_J/(2J+1) \propto \exp(-E_J/kT)$ , where  $E_J$  is the energy of the  $J$ th rotational state above the ground rotational state. It is therefore useful to plot  $\ln[N_J/(2J+1)]$  versus  $E_J/k$ . If the data points fall along a straight line, then LTE is probably a valid approximation, and the gas temperature is obtained as the inverse of the slope of the line. If the points do not follow a straight line in such a plot, then LTE at a single temperature is not a valid assumption.

An LTE distribution of CO among rotational levels requires some minimum gas density so that collisional rates exceed spontaneous rotational decay rates. Because the rate of spontaneous emission,  $A_J$ , is proportional to  $J^3$ , the density required for thermalization is higher for higher rotational states. In general, rotational level populations of CO must be obtained by solution of the equations of statistical equilibrium. Such calculations have been carried out by, for example, Storey *et al.* (1981), McKee *et al.* (1982), and Viscuso and Chernoff (1988). McKee *et al.* give a useful analytic approximation which allows rapid calculation of the departure coefficient,  $b_J = n_J/n_J^*$ , for any kinetic temperature and total gas density. Here,  $n_J$  is the actual number density of CO in level  $J$  and  $n_J^*$  is the number density predicted by the Boltzmann equation. The McKee *et al.* (1982) calculation is simplified by the assumptions that infrared pumping is negligible and that only the ground vibrational state contains a significant population. Viscuso and Chernoff (1988), using improved rate coefficients for the  $\text{H}_2 + \text{CO}$  system, found only rather small differences from the results of McKee *et al.* We have made use of the analytic approximation of McKee *et al.* (1982) in an attempt to place limits on the kinetic temperature and total gas density for the various components of gas we have found toward GL 2591.

Care must be taken in deducing gas properties from observed CO populations in a restricted range of energy levels. The difficulty in obtaining reliable gas properties from radio observations is particularly acute because often only the  $J=1-0$  and  $J=2-1$  transitions are observed. As an illustration, Figure 6 shows the calculated populations for rotational levels up to  $J=23$  in the case of  $T_{\text{kin}} = 1000 \text{ K}$ . We have plotted  $\ln[n_J/(2J+1)]$  versus  $E_J/k$  so that the calculations can be conveniently compared to our observed rotational populations. The zero point of the vertical scale in Figure 6 is arbitrary. It can be seen from Figure 6 that densities exceeding  $10^7 \text{ cm}^{-3}$  are required for a Boltzmann distribution of populations to be achieved over the entire range of rotational levels, so that  $T_{\text{rot}} = T_{\text{kin}}$ . At  $n \approx 10^6 \text{ cm}^{-3}$ , the lower  $J$  levels alone have

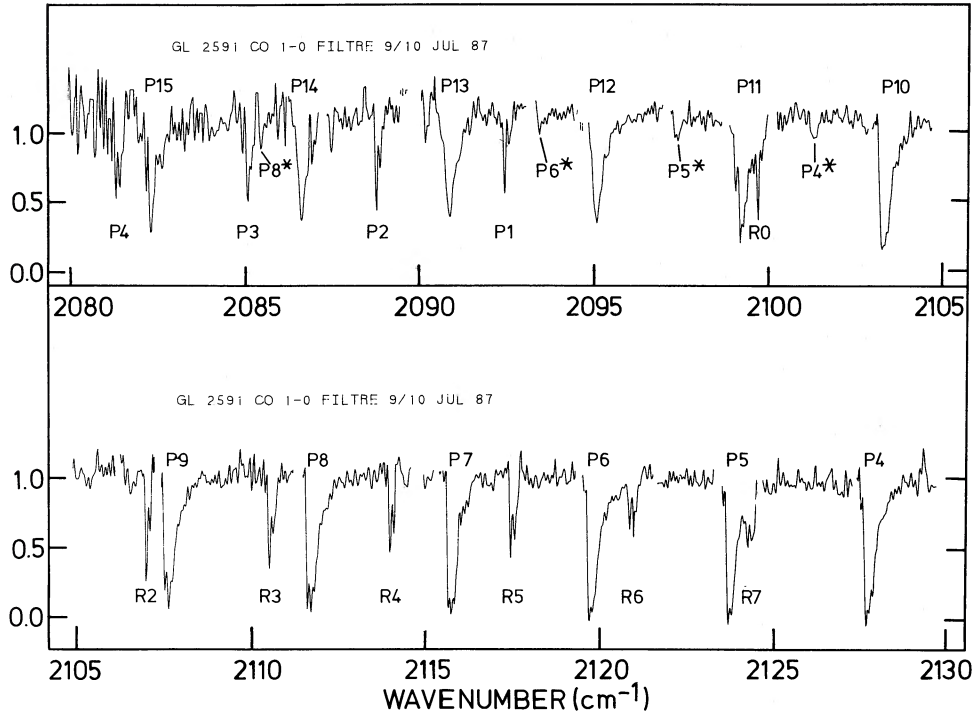


FIG. 4a

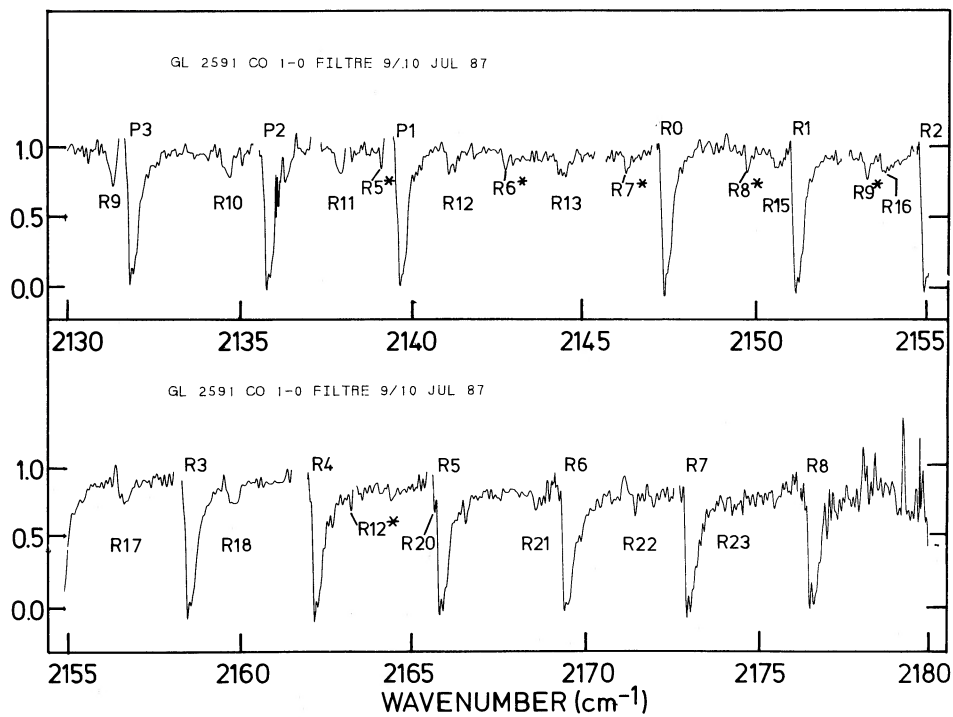


FIG. 4b

FIG. 4.—The spectrum of GL 2591 is divided by the spectrum of  $\alpha$  Lyr to obtain a ratioed spectrum. Gaps in the spectrum correspond to saturated telluric features. Lines of  $^{12}\text{CO}$  are labeled above the spectrum, lines of  $^{13}\text{CO}$  are labeled below the spectrum, and lines of vibrationally excited  $^{12}\text{CO}$  ( $v = 1-2$ ) are indicated with an asterisk (e.g.,  $R5^*$ ).

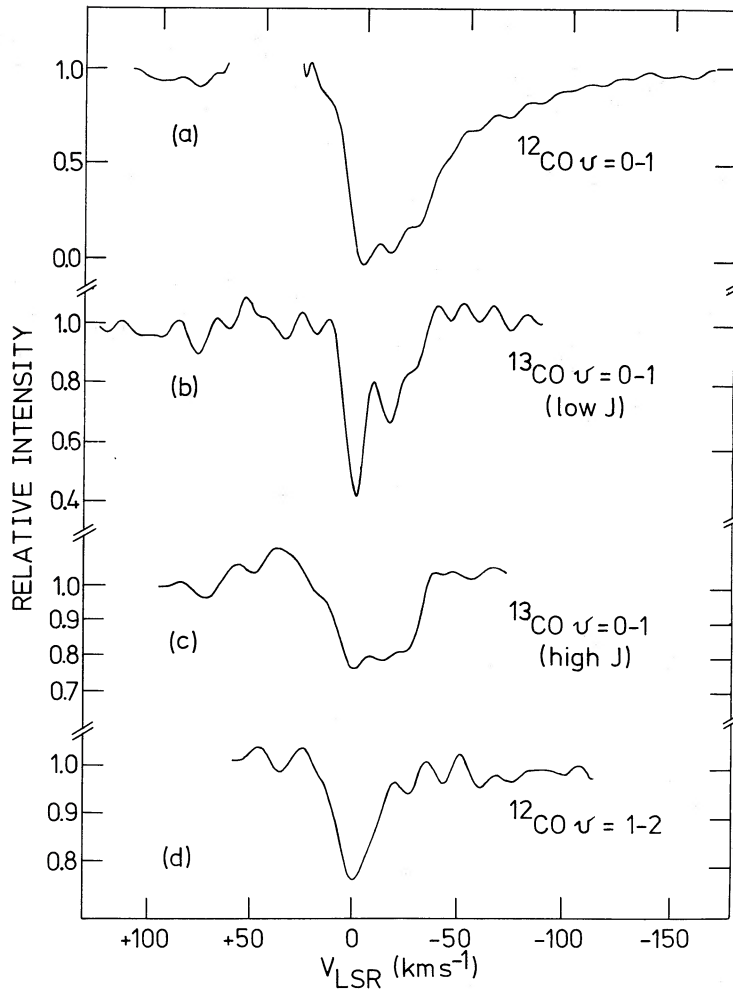


FIG. 5.—Average kinematic profiles have been obtained from the ratio spectrum using those lines which are free of strong telluric features. The  $^{12}\text{CO } v = 0-1$  profile, (a), is an average over the P8, P7, P4, P3, P1, R0, R1, R6, and R7 lines. The  $^{13}\text{CO } v = 0-1$  lines have been separated into low  $J$  and high  $J$  regimes for reasons explained in the text. The low  $J$  average, (b), is over the P2, P1, R3, and R5 lines, while the high  $J$  average, (c), is over the R10, R11, R12, R13, R15, R16, R17, and R18 lines. The  $^{12}\text{CO } v = 1-2$  profile, (d), is an average over the P4, R6, R7, R8, and R9 lines. The three velocity features seen in (a), (b), and (c) have the LSR velocities  $-11 \text{ km s}^{-1}$ ,  $-28 \text{ km s}^{-1}$ , and  $-38 \text{ km s}^{-1}$ .

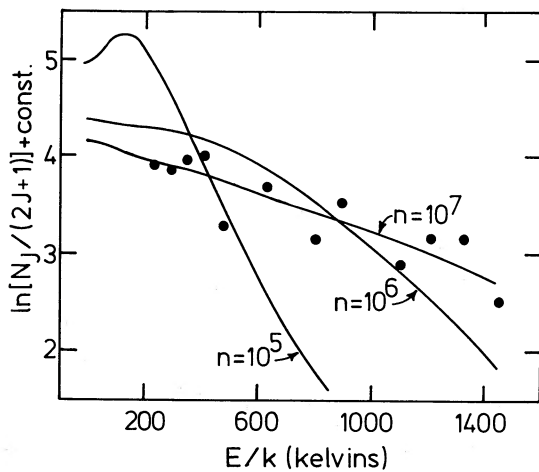


FIG. 6.—Theoretically calculated rotational CO populations per sublevel are plotted against rotational energy for a gas kinetic temperature of 1000 K. The results for three gas densities,  $10^5 \text{ cm}^{-3}$ ,  $10^6 \text{ cm}^{-3}$ , and  $10^7 \text{ cm}^{-3}$ , are shown. The observations for the high  $J$  levels of the  $-11 \text{ km s}^{-1}$  component of  $^{13}\text{CO}$ , shown as closed circles, have been shifted vertically to overlie the  $10^7 \text{ cm}^{-3}$  theoretical curve.

$T_{\text{rot}} > T_{\text{kin}}$  (shallower slope) while the higher  $J$  levels alone have  $T_{\text{rot}} < T_{\text{kin}}$  (steeper slope). At densities of  $n \approx 10^5 \text{ cm}^{-3}$ , low  $J$  levels exhibit population inversion, while the higher  $J$  levels mimic a Boltzmann distribution with  $T_{\text{rot}}$  much less than  $T_{\text{kin}}$ . The dependence of level populations on gas density is qualitatively similar over the entire range of kinetic temperatures, 200 K to 4000 K, for which we have made calculations.

a) Gas at  $v_{\text{LSR}} = -11 \text{ km s}^{-1}$

Line positions, measured equivalent widths, and calculated column densities are shown in Table 1. The LSR velocity is obtained from the observed velocity shift by removing Earth's velocity relative to the LSR for the date of observation ( $27.3 \text{ km s}^{-1}$ ). Figure 7 shows  $\ln[N_J / (2J + 1)]$  plotted against  $E_J/k$  for the  $^{13}\text{CO}$  absorption lines using the column densities of Table 1. It is evident from Figure 7 that a single straight line is a poor representation of the data. The distribution of points has a break at  $E_J/k \approx 100 \text{ K}$ . We see from the figure, however, that the low  $J$  points can be fitted by one straight line and the high  $J$  points can be fitted by a second line of shallower slope. A least-squares linear fit to the lower rotational states,  $J \leq 6$ , is displayed in Figure 7. While the fit, which indicates a tem-

TABLE 1  
 $^{13}\text{CO}$  ( $v = 0-1$ ) ABSORPTION LINES AT  $v_{\text{LSR}} = -11 \text{ km s}^{-1}$

Line	Observed $\omega$ ( $\text{cm}^{-1}$ )	Rest $\omega$ ( $\text{cm}^{-1}$ )	Velocity Shift ( $\text{km s}^{-1}$ )	Equivalent Width ( $\text{cm}^{-1}$ )	$N_J^a$ ( $10^{16} \text{ cm}^{-2}$ )	$N_J^b$ ( $10^{16} \text{ cm}^{-2}$ )
P1	2092.655	2092.391	37.82	0.04344	1.52	2.34
P2	2088.949	2088.682	38.32	0.05515	1.61	2.98
R2	2107.166	2106.898	38.13	0.06254	1.20	2.55
P3	2085.204	2084.942	37.67	0.05206	1.42	2.50
R3	2110.711	2110.442	38.21	0.05773	1.16	2.23
P4	2081.428	2081.168	37.46	0.03838	1.01	1.46
R4	2114.221	2113.953	38.01	0.04238	0.878	1.32
R5	2117.696	2117.431	37.51	0.03733	0.785	1.11
R6	2121.149	2120.875	38.73	0.02566	0.546	0.678
R9	2131.313	2131.004	43.47	0.01619	0.350	
R10	2134.560	2134.313	34.70	0.01694	0.367	
R11	2137.892	2137.588	42.63	0.02048	0.444	
R12	2141.100	2140.828	38.09	0.02302	0.500	
R13	2144.277	2144.033	34.12	0.01209	0.263	
R15	2150.542	2150.341	28.03	0.02071	0.450	
R16	2153.718	2153.442	38.43	0.01803	0.391	
R17	2156.781	2156.509	37.80	0.01378	0.299	
R18	2159.812	2159.540	37.75	0.02117	0.459	
R20	2165.759	2165.497	36.26	0.01247	0.270	
R21	2168.651	2168.422	31.67	0.01715	0.370	
R22	2171.554	2171.312	33.42	0.01764	0.380	
R23	2174.356	2174.166	26.20	0.00943	0.203	

<sup>a</sup> Calculated for optically thin lines.

<sup>b</sup> Obtained from a curve-of-growth analysis.

perature of 45 K, is reasonably good, the distribution of points shows some curvature. We, therefore, set aside the assumption of optical thinness in the low  $J$  lines and carried out a curve of growth analysis, following Spitzer (1978), in which the line width was taken as a free parameter. Column densities computed for a line width (FWHM) of  $6.5 \text{ km s}^{-1}$  gave the best linear fit. This case is shown in Figure 8 and the column densities are listed in the last column of Table 1. The slope of the line yields a rotational temperature of  $38 \pm 3 \text{ K}$ , where  $1 \sigma$

errors on the slope are quoted.<sup>2</sup> The nine lines with  $J \leq 6$  have a mean measured line width (FWHM) of  $11.9 \pm 2.6 \text{ km s}^{-1}$ , significantly greater than the instrumental line width of  $8.0 \text{ km s}^{-1}$

<sup>2</sup> The errors which are quoted for temperatures and total CO column densities are due to the actual scatter in the  $N_J$ 's. A measure of the uncertainty in the individual  $N_J$ 's is given by the minimum detectable equivalent width,  $W_{\text{min}} = \text{resolution}/\text{signal-to-noise}$ . Adopting a  $1 \sigma$  S/N of 90,  $W_{\text{min}} = 0.00063 \text{ cm}^{-1}$ , corresponding to a minimum detectable column density per  $J$  level of  $\sim 2 \times 10^{14} \text{ cm}^{-2}$ .

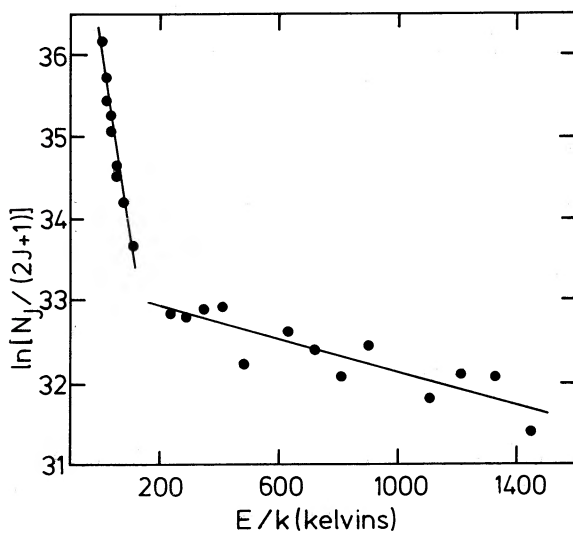


FIG. 7

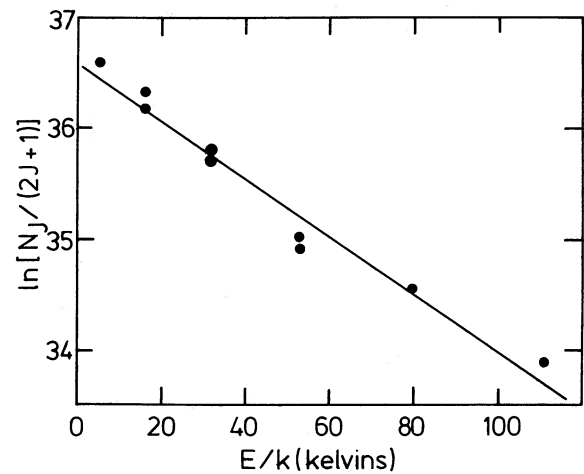


FIG. 8

FIG. 7.— $^{13}\text{CO}$  column densities in each rotational sublevel are plotted as a function of the rotational energy in kelvins for the absorption lines at  $v_{\text{LSR}} = -11 \text{ km s}^{-1}$ . Column densities were computed on the assumption that the lines are optically thin.

FIG. 8.—The same as Fig. 7 except that only lines with  $J \leq 6$  are plotted, and column densities were computed using a curve-of-growth analysis with line width (FWHM) of  $6.5 \text{ km s}^{-1}$ . The line is a least-squares fit and indicates a rotational temperature of  $38 \pm 3 \text{ K}$ .

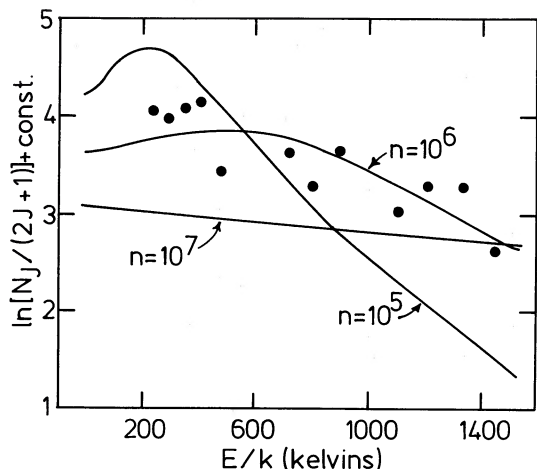


FIG. 9.—The same as Fig. 6 but for  $T_{\text{kin}} = 3000$  K. The density of  $5 \times 10^5 \text{ cm}^{-3}$  provides a reasonable fit to the high  $J$  levels of the  $-11 \text{ km s}^{-1}$  gas.

$\text{s}^{-1}$ . The intrinsic FWHM of these lines, using  $\Delta v^2 \approx \Delta v_{\text{obs}}^2 - \Delta v_{\text{inst}}^2$ , is  $8.8 \pm 2.6 \text{ km s}^{-1}$ , somewhat larger than, but compatible with, the line width which gives the best linear fit to the curve of growth analysis.

The slope of the line through the higher rotational states, shown in Figure 7, yields a high rotational temperature of  $1012(+201, -143) \text{ K}$ . The lines with  $J \geq 9$  are definitely optically thin, so that a curve-of-growth analysis is unnecessary. The mean measured line width (FWHM) of the lines with  $J \geq 9$  is  $15.2 \pm 3.6 \text{ km s}^{-1}$ , so that their intrinsic line width is  $12.9 \pm 3.6 \text{ km s}^{-1}$ , larger than the width of the low  $J$  lines.

The observed CO populations of the higher rotational levels ( $J \geq 9$ ) for the  $v_{\text{LSR}} = -11 \text{ km s}^{-1}$  component are plotted in Figure 6, where it is easily seen that the best fit for  $T_{\text{kin}} = 1000 \text{ K}$  is given by gas at  $n \geq 10^7 \text{ cm}^{-3}$ . Because of scatter in the data, however, an acceptable fit can be achieved for a higher kinetic temperature. From a similar plot for  $T_{\text{kin}} = 3000 \text{ K}$  (Fig. 9), it can be seen that  $T = 3000 \text{ K}$  and  $n = 5 \times 10^5 \text{ cm}^{-3}$  fit the data fairly well. Temperatures significantly lower than  $1000 \text{ K}$  are not allowed because the slope is too steep for any density. We conclude that the high  $J$  CO absorption lines are most likely formed in gas with  $T \approx 1000 \text{ K}$  and  $n \geq 10^7$ , but that gas temperatures as high as  $3000 \text{ K}$  cannot be ruled out.

Once the excitation temperature is known, the Boltzmann equation in the form  $N_J/N = [g_J/Z(T)] \times \exp(-E_J/kT)$  allows the calculation of the total CO column density (in some vibrational state) from the column density of CO in any rotational state (of the specified vibrational state). We have calculated  $^{13}\text{CO}$  column densities from each rotational state and averaged the results to find  $N_{\text{cold}}(^{13}\text{CO}) = (1.2 \pm 0.2) \times 10^{17} \text{ cm}^{-2}$  for the cold gas at  $-11 \text{ km s}^{-1}$ , and  $N_{\text{hot}}(^{13}\text{CO}) = (9.3 \pm 1.9) \times 10^{16} \text{ cm}^{-2}$  for the hot gas. The fact that the hot and cold CO have comparable abundances may seem, at first, surprising, in view of the much stronger lines produced in the cold gas (low  $J$  lines). The hot gas is, however, distributed over many more rotational states so that individual lines are weaker although the total abundance is high.

#### b) Gas at $v_{\text{LSR}} = -28 \text{ km s}^{-1}$

Fifteen lines of  $^{13}\text{CO}$  at  $v_{\text{LSR}} = -28 \text{ km s}^{-1}$  are visible in Figure 4. The average width (FWHM) of these lines is  $15.8 \text{ km s}^{-1}$ . After correction for the instrumental line width, the intrinsic line width of this component is  $12.5 \pm 3.0 \text{ km s}^{-1}$ . The lines are sufficiently weak that a curve-of-growth analysis is unnecessary. We have calculated column densities using the optically thin relation between  $W_\omega$  and  $N_J$  given above. The results are shown in Table 2. When  $\ln[N_J/(2J+1)]$  is plotted against  $E/k$  (Fig. 10), the distribution of points is well fitted by a straight line corresponding to a temperature of  $201(+12, -10) \text{ K}$ .

Theoretical (non-LTE) rotational populations for  $T_{\text{kin}} = 200 \text{ K}$  (Fig. 11) imply a gas density of  $n \geq 10^7 \text{ cm}^{-3}$ . The temperature is rather well constrained because higher  $T$  gas, even at lower densities, cannot fit the low  $J$  and high  $J$  points simultaneously, while gas with  $T_{\text{kin}} < 200 \text{ K}$  results in too steep a slope. A total  $^{13}\text{CO}$  column density is calculated from each  $N_J$  of Table 2, and these are averaged to obtain  $N(^{13}\text{CO}) = (1.1 \pm 0.3) \times 10^{17} \text{ cm}^{-2}$  for this velocity component.

#### c) Vibrationally Excited $^{12}\text{CO}$

Table 3 lists the line positions, equivalent widths, and lower state column densities for all of the measured CO  $v = 1-2$  transitions. Column densities were calculated using the optically thin expression relating  $W_\omega$  and  $N_J$ . A plot of  $\ln[N_J/(2J+1)]$  versus  $E/k$  allows us to obtain a rotational temperature

TABLE 2  
 $^{13}\text{CO}$  ( $v = 0-1$ ) ABSORPTION LINES AT  $v_{\text{LSR}} = -28 \text{ km s}^{-1}$

Line	Observed $\omega$ ( $\text{cm}^{-1}$ )	Rest $\omega$ ( $\text{cm}^{-1}$ )	Doppler Shift ( $\text{km s}^{-1}$ )	Equivalent Width ( $\text{cm}^{-1}$ )	$N_J$ ( $10^{15} \text{ cm}^{-2}$ )
P1	2092.771	2092.391	54.46	0.01733	6.069
P2	2089.057	2088.682	53.82	0.03210	9.391
R2	2107.274	2106.898	53.50	0.03346	6.447
P3	2085.302	2084.942	51.76	0.03347	9.161
R3	2110.823	2110.442	54.13	0.04315	8.707
P4	2081.539	2081.168	53.45	0.04264	11.28
R4	2114.331	2113.953	53.61	0.03150	6.523
R5	2117.812	2117.431	53.93	0.04493	9.453
R9	2131.442	2131.004	61.62	0.03807	8.222
R10	2134.731	2134.313	58.70	0.02992	6.477
R11	2138.009	2137.588	59.03	0.02386	5.174
R12	2141.279	2140.828	63.15	0.01717	3.727
R13	2144.389	2144.033	49.78	0.01249	2.712
R15	2150.733	2150.341	54.66	0.00955	2.074
R16	2153.845	2153.442	56.09	0.00961	2.086

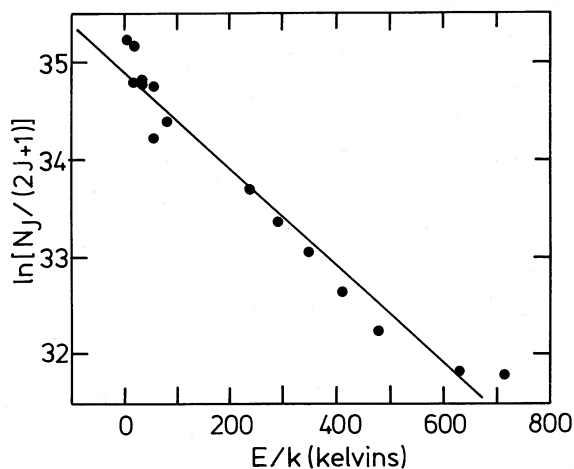


FIG. 10

FIG. 10.—The same as Fig. 7 except that column densities of the  $^{13}\text{CO}$  absorption lines at  $v_{\text{LSR}} = -28 \text{ km s}^{-1}$  are plotted. The linear fit indicates a CO rotational temperature of  $201(+12, -10) \text{ K}$ .

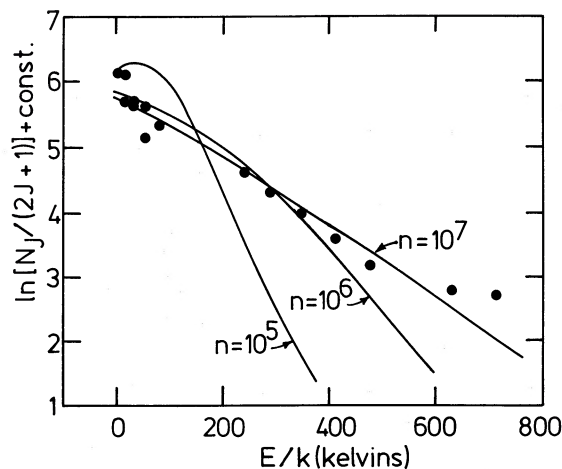


FIG. 11

FIG. 11.—The same as Fig. 6 but for  $T_{\text{kin}} = 200 \text{ K}$ . The observed abundances for the  $-28 \text{ km s}^{-1}$  gas, plotted as filled circles, are well fitted by the  $n = 10^7 \text{ cm}^{-3}$  curve.

for  $^{12}\text{CO}$  in the first excited vibrational state. In Figure 12, the data of Table 3 are plotted, with the *P* and *R* branch column densities for the same rotational level being averaged. The rotational temperature deduced from the slope of the line is  $640(+220, -130) \text{ K}$ . This temperature agrees, to  $1 \sigma$ , with the rotational temperature of  $1012 \text{ K}$  for the hot  $^{13}\text{CO}$  gas. We conclude, therefore, that the vibrationally excited  $^{12}\text{CO}$  and the hot  $^{13}\text{CO}$  coexist.

The existence of a substantial population of vibrationally excited CO implies that the physical conditions in the absorbing gas are extreme. Because the  $v = 1$  state lies  $\sim 3000$  kelvins above the ground vibrational state, high gas temperatures are required to collisionally populate the  $v = 1$  state. Furthermore, because the spontaneous decay rates from vibrationally excited states are so very fast (e.g.,  $30.6 \text{ s}^{-1}$  for the transition [ $v = 1, J = 0$ ] to [ $v = 0, J = 1$ ]), extremely high densities are required to maintain the population of vibrationally excited levels. If the gas is optically thin in the vibrational emission lines, a density exceeding  $10^{10} \text{ cm}^{-3}$  is required to thermalize the  $v = 1$  level.

Using the rotational temperature of  $640 \text{ K}$  for the vibrationally excited CO, the Boltzmann equation allows the total column density of the state  $v = 1$  to be obtained from the column density in any rotational level. Applying the Boltzmann equation to each  $N_J$  of Table 3 and averaging the results, we find  $N_{v=1}(^{12}\text{CO}) = (3.9 \pm 0.7) \times 10^{16} \text{ cm}^{-2}$ . The degree of

thermalization of the vibrational levels could be determined if the vibrational temperature of the CO were known. Similar values for the rotational and vibrational temperatures would

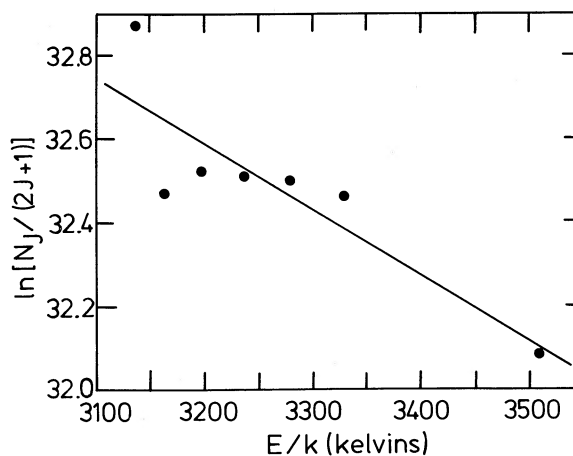


FIG. 12.— $^{12}\text{CO}$  ( $v = 1-2$ ) column densities per sublevel are plotted against excitation energy. *P* and *R* branch column densities for the same rotational level have been averaged. The slope of the line yields a rotational temperature of  $634(+216, -128) \text{ K}$ .

TABLE 3  
 $^{12}\text{CO}$  ( $v = 1-2$ ) ABSORPTION LINES

Line	Observed $\omega$ ( $\text{cm}^{-1}$ )	Rest $\omega$ ( $\text{cm}^{-1}$ )	Doppler Shift ( $\text{km s}^{-1}$ )	Equivalent Width ( $\text{cm}^{-1}$ )	$N_J$ ( $10^{15} \text{ cm}^{-2}$ )
P4	2101.596	2101.343	36.10	0.01320	1.697
P5	2097.68	2097.394	40.87	0.01466	1.847
R5	2139.154	2138.911	34.06	0.00901	0.9212
P6	2093.657	2093.411	35.22	0.01161	1.444
R6	2142.737	2142.473	36.93	0.01947	2.012
R7	2146.239	2145.999	33.53	0.01894	1.972
P8	2085.598	2085.343	36.67	0.01911	2.343
R8	2149.741	2149.489	35.14	0.01981	2.072
R9	2153.210	2152.942	37.32	0.02263	2.376
R12	2163.325	2163.083	33.54	0.02017	2.128

support thermalization. We can obtain a vibrational temperature from the relative populations of the  $v = 0$  and  $v = 1$  states by applying Boltzmann's equation in the form

$$N_1/N_0 = \exp(-3082/T_{\text{vib}}),$$

where  $N_1$  and  $N_0$  are the CO column densities in the first excited and the ground vibrational states. Before a ratio can be taken, however, the abundance of  $^{12}\text{CO}$  in the  $v = 0$  state must be obtained from  $^{13}\text{CO}$  ( $v = 0$ ) by the use of an appropriate isotopic abundance ratio. The  $^{12}\text{CO}/^{13}\text{CO}$  ratio in interstellar clouds exhibits a range of values from  $\sim 20$  to  $\sim 140$ . We choose to use  $^{12}\text{CO}/^{13}\text{CO} = 60$ , the mean ratio obtained by Wannier (1980). If the solar abundance ratio of 89 applies, as found, for example, by Scoville *et al.* (1983) for the BN object, our  $^{12}\text{CO}$  column densities must be increased by the factor 1.48. The result, using  $^{12}\text{CO}/^{13}\text{CO} = 60$ , is a vibrational temperature of 620 K. The vibrational temperature is, therefore, quite similar to the rotational temperature of the gas. We must emphasize that the scatter in the  $^{12}\text{CO}$  ( $v = 1-2$ ) line data is large. The data are, however, consistent with thermalization of the  $v = 0$  and  $v = 1$  levels. It should be noted that only  $\sim 1\%$  of CO is vibrationally excited.

#### d) The Broad Velocity $^{12}\text{CO}$

Measurement of the high-velocity wings of the  $^{12}\text{CO}$  lines is hampered by the superposition of the two saturated  $^{12}\text{CO}$  features at  $-11$  and  $-28 \text{ km s}^{-1}$ . We estimate by inspection that the portions of the  $^{12}\text{CO}$  lines to the blue of  $-40 \text{ km s}^{-1}$  will be well clear of the wings of the  $-28 \text{ km s}^{-1}$  feature. In order to obtain information on possible variation of gas properties with velocity, we divided the high-velocity wing of the  $^{12}\text{CO}$  feature into four velocity components:  $-54 < v_{\text{LSR}} \leq -40 \text{ km s}^{-1}$  (component "a"),  $-69 < v_{\text{LSR}} \leq -54 \text{ km}$

$\text{s}^{-1}$  (component "b"),  $-79 < v_{\text{LSR}} \leq -69 \text{ km s}^{-1}$  (component "c"), and  $-130 < v_{\text{LSR}} \leq -79 \text{ km s}^{-1}$  (component "d"). These particular velocity ranges were chosen, by inspection of the  $^{12}\text{CO}$  lines in the clearest region of the spectrum ( $\sim 2130-2150 \text{ cm}^{-1}$ ), to coincide with bumps in the line profile. The lowest velocity range contains that portion of the  $-38 \text{ km s}^{-1}$  component which is clear of the strong velocity component centered at  $-28 \text{ km s}^{-1}$ . Our analysis, however, shows no difference in gas properties for the different velocity ranges, so the choice of velocity intervals is not critical.

Equivalent widths were obtained for each of these "components" and column densities calculated using the optically thin approximation. The results are given in Table 4. Plots of  $\ln[N_J/(2J+1)]$  versus  $E/k$  are shown in Figure 13a-d. Perhaps the most striking feature of Figure 13 is the upward curvature of the lower  $J$  points. Clearly, the high-velocity gas cannot be well described by a Boltzmann distribution at a single gas temperature. Although the scatter in the plots increases for the higher velocity components due to a weaker signal, all four velocity intervals can be fitted by the same curve. In other words, we have the remarkable result that the physical properties of the outflowing gas are the same at each velocity. To improve the signal-to-noise ratio, we have added the column densities for the velocity intervals a, b, and c, with the result shown in Figure 14. An interesting feature of Figures 13 and 14 is the linearity of the high  $J$  point distribution. Rotational levels with  $J \geq 7$  are well fitted by a line of  $T = 504 \pm 30 \text{ K}$  (Fig. 15). The physical significance of this temperature is, however, unclear. The curvature of the point distribution in Figures 13 and 14 cannot be due to the effects of optical depth because the broad feature is resolved in velocity and clearly unsaturated. In any case, the equivalent widths of the high-velocity components vary little with  $J$  so that the

TABLE 4  
EQUIVALENT WIDTHS AND COLUMN DENSITIES OF THE HIGH-VELOCITY  $^{12}\text{CO}$  GAS

LINE	VELOCITY RANGE ( $\text{km s}^{-1}$ )							
	-40 to -54		-54 to -69		-69 to -79		-79 to -130	
	$W_\omega^a$	$N_J^b$	$W_\omega^a$	$N_J^b$	$W_\omega^a$	$N_J^b$	$W_\omega^a$	$N_J^b$
R0	0.0554	0.6160	0.0271	0.3013	0.0081	0.0901	0.0164	0.1824
P1	0.0483	1.619	0.0225	0.7541	0.0124	0.4156	0.0297	0.9954
R1	0.0604	1.005	0.0270	0.4492	0.0148	0.2462	0.0262	0.4359
R2	0.0639	1.178	0.0337	0.6214	0.0144	0.2655	0.0494	0.9109
P3	0.0595	1.559	0.0378	0.9901	0.0156	0.4086	0.0454	1.189
R3	0.0676	1.305	0.0457	0.8825	0.0209	0.4036	0.0543	1.049
P4	0.0711	1.800	0.0406	1.028	0.0177	0.4481	0.0431	1.091
R4	0.0635	1.258	0.0403	0.7986	0.0213	0.4221	0.0648	1.284
P5	0.0570	1.415	0.0356	0.8835	0.0176	0.4368	0.1158	2.874
R5	0.0671	1.351	0.0464	0.9141	0.0197	0.3966	0.0453	0.9121
P6	0.0604	1.480	0.0461	1.019	0.0151	0.3700	0.0368	0.9018
R6	0.0696	1.416	0.0494	1.005	0.0279	0.5677	0.0853	1.736
P7	0.0662	1.608	0.0294	0.7143	0.0175	0.4252	0.0315	0.7653
R7	0.0716	1.468	0.0501	1.027	0.0137	0.2808	0.0380	0.7788
P8	0.0717	1.732	0.0454	1.097	0.0208	0.5024	0.0482	1.164
R8	0.0768	1.582	0.0514	1.059	...	...	0.0292	0.6014
P9	0.0608	1.463	0.0399	0.9599	0.0200	0.4811	0.0447	1.075
R9	0.0509	1.052	...	...	...	...	...	...
P10	0.0654	1.569	0.0376	0.9019	0.0186	0.4461	0.0475	1.139
P11	0.0606	1.451	0.0375	0.8979	0.0190	0.4550	0.0974	2.332
P12	0.0536	1.282	0.0415	0.9925	0.0185	0.4424	0.0396	0.9470
P13	0.0563	1.346	0.0336	0.8032	0.0163	0.3896	0.0181	0.4327
P14	0.0522	1.248	0.0397	0.9488	0.0175	0.4182	0.0796	1.902
P15	0.0456	1.090	0.0237	0.5665	0.0167	0.3992	0.0255	0.6096

<sup>a</sup> Equivalent width, in units of  $\text{cm}^{-1}$ .

<sup>b</sup> Column density in rotational state  $J$ , in units of  $10^{16} \text{ cm}^{-2}$ .

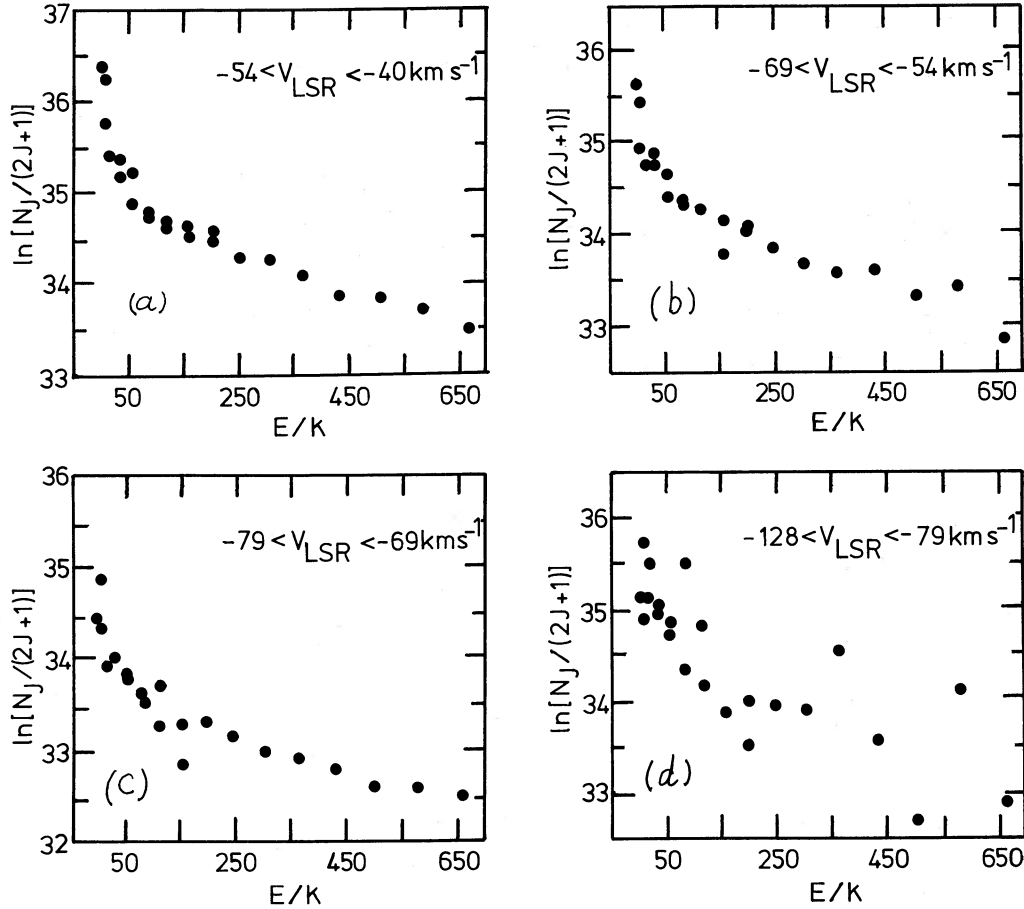


FIG. 13.—Column densities per sublevel are plotted against  $E/k$  for the high-velocity  $^{12}\text{CO}$  absorption. The broad feature is divided into four velocity intervals which are plotted separately.

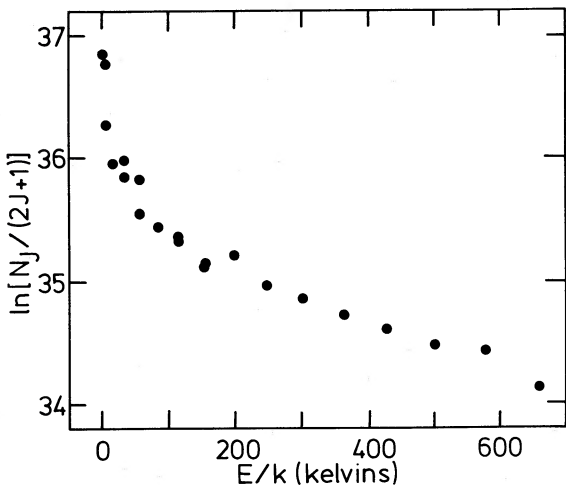


FIG. 14

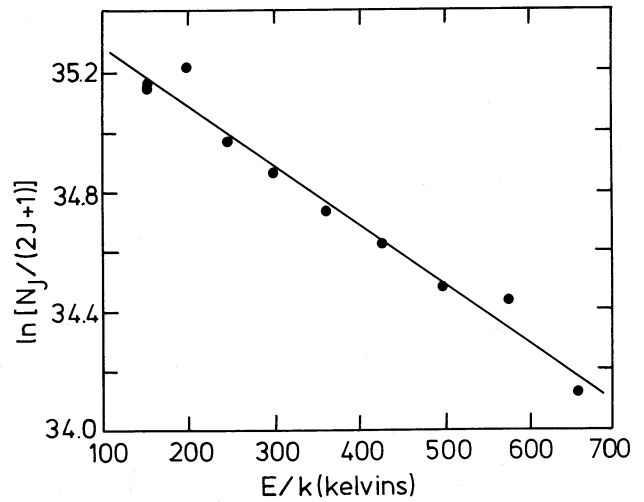


FIG. 15

FIG. 14.—The same as Fig. 13, but column densities in the velocity intervals (a), (b), and (c) have been added to improve the signal-to-noise ratio.  
 FIG. 15.—The same as Fig. 14, except that only higher  $J$  points,  $J \geq 7$ , are shown. The least-squares linear fit implies a rotational temperature of  $504 \pm 30 \text{ K}$ .

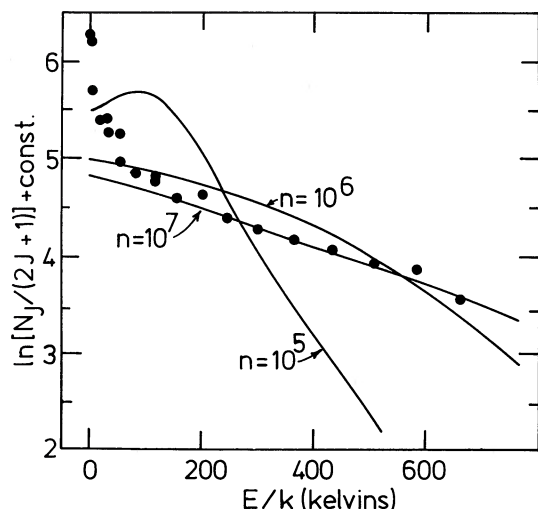


FIG. 16.—The same as Fig. 6 but for a kinetic temperature of 500 K. Data for the high-velocity CO (from Fig. 14) are plotted as filled circles. An excellent fit to levels with  $J \geq 7$  is provided by the  $n = 10^7 \text{ cm}^{-3}$  curve, but no density fits the low  $J$  data points.

effect of a small optical depth will raise each point but will not reduce the curvature. The non-Boltzmann distribution of the rotational populations appears to be telling us that either the gas is not uniform in temperature and/or density, or, if the gas is uniform, the CO is not in local thermodynamic equilibrium.

The rotational populations of the high-velocity gas are difficult to understand as a departure from LTE. Our calculations show that the upward curvature for low  $J$  levels (Fig. 14) is not predicted for any pair  $(T_{\text{kin}}, n)$ . An excellent fit to high  $J$  levels,  $J \geq 7$ , is provided by  $T = 500 \text{ K}$  and  $n \geq 10^7 \text{ cm}^{-3}$  (Fig. 16). The theoretical curves in Figure 16 are obtained under the assumption that the gas is optically thin in the rotational lines. We have confirmed that the gas is optically thin by computing the line optical depths,  $\tau_J$ , using equation (4.1) of McKee *et al.* (1982). We find  $\tau_J \leq 0.1$  for each  $J$ .

Another possibility for the high-velocity gas is that infrared pumping may be overpopulating low  $J$  levels. This would be the reverse of the normally expected effect (e.g., Carroll and Goldsmith 1981). It has, however, been pointed out recently by Schonberg (1988), with reference to CO in stellar envelopes, that the situation can be reversed when direct radiation from dust is important. A clarification of the importance of infrared pumping will require a careful treatment of the radiative transfer problem.

The simplest explanation for the unusual distribution of populations is that the high-velocity gas is nonuniform. We envision an expanding neutral wind possessing a gradient in temperature, velocity, and density. Detailed modeling of the

wind is beyond the scope of this paper, but the CO data presented here will provide strong constraints on the wind properties (e.g., velocity law, temperature structure, density gradient).

#### e) Gas at $v_{\text{LSR}} = +1 \text{ km s}^{-1}$

The red wings with low rotation quantum numbers display a slight non-Gaussian slope which suggests a weak blended feature. Decomposition of the CO profiles shows a component at  $v_{\text{LSR}} = +0.9 \text{ km s}^{-1}$  which is detectable in lines from P3 to R3 but disappears for larger rotational quantum numbers. The absence of absorption for  $J > 3$  suggests that the gas is very cold ( $T \approx 10 \text{ K}$ ). The velocity of this feature coincides with a weak component at  $1 \text{ km s}^{-1}$  detected by Lada *et al.* (1984) in millimetric CO and confirms the existence of another “clump” along the line of sight to the infrared source.

#### IV. DISCUSSION

The properties of the various gas components in the line of sight to GL 2591 were presented in §§ II and III above. The gas properties are summarized in Table 5. Column densities of  $^{12}\text{CO}$  in Table 5 have been obtained from  $^{13}\text{CO}$  column densities by assuming a ratio  $^{12}\text{CO}/^{13}\text{CO} = 60$ . As Table 5 shows, we identify four physically distinct components: (1) cold ( $38 \text{ K}$ ) gas at  $v_{\text{LSR}} = -11 \text{ km s}^{-1}$ , (2) hot gas ( $\sim 1000 \text{ K}$ ) at the same velocity, (3) warm ( $200 \text{ K}$ ) gas at  $v_{\text{LSR}} = -28 \text{ km s}^{-1}$ , and (4) a high-velocity wind with velocity up to  $\sim -130 \text{ km s}^{-1}$ . The gas with  $T_{\text{rot}} \approx 1000 \text{ K}$  found from the high rotational levels of  $^{13}\text{CO}$  (No. 2a in Table 5) is almost certainly the same gas which is seen in lines of vibrationally excited  $^{12}\text{CO}$  (No. 2b in Table 5). The velocities of the cold gas (component 1) and hot gas (component 2) coincide within the errors although we cannot, of course, rule out the possibility that the formal 2 or 3  $\text{km s}^{-1}$  velocity difference between the two components is real. We do not give a column density for the high-velocity CO (component 4 of Table 5) because this gas appears to be non-uniform. A physical model of this wind will be required before column densities can be deduced.

We showed in § III that the low  $J$  absorption lines with  $v_{\text{LSR}} = -11 \text{ km s}^{-1}$  are formed in cold gas with  $T = 38 \text{ K}$ , while the high  $J$  absorption lines with the same velocity are formed in hot gas with  $T \approx 1000 \text{ K}$ . The existence of gas with two temperatures has a straightforward physical explanation: The  $38 \text{ K}$  gas is very likely the cold core of the molecular cloud within which GL 2591 is embedded, while the  $1012 \text{ K}$  gas is near the infrared source and is warmed by its radiation. There is a puzzling discrepancy of several  $\text{km s}^{-1}$  between the velocity of the absorption feature and the central velocity of the  $^{12}\text{CO}$  emission toward GL 2591 ( $v_{\text{LSR}} \approx -5 \text{ km s}^{-1}$ ; Bally and Lada 1983). Lada *et al.* (1984) suggest, however, on the basis of differences between 11 m and 12 m telescope results, that the

TABLE 5  
SUMMARY OF GAS PROPERTIES

No.	Indicator	$v_{\text{LSR}}$ ( $\text{km s}^{-1}$ )	$T_{\text{ex}}$ (K)	$N(^{13}\text{CO})$ ( $10^{17} \text{ cm}^{-2}$ )	$N(^{12}\text{CO})$ ( $10^{18} \text{ cm}^{-2}$ )
1	$^{13}\text{CO } v = 0-1, J \leq 6$ (9 lines)	$-10.7 \pm 0.4$	$38 \pm 3$	$1.2 \pm 0.2$	$7.2 \pm 1.2^a$
2a	$^{13}\text{CO } v = 0-1, J \geq 9$ (13 lines)	$-8 \pm 5$	$1010^{+220}_{-140}$	$0.93 \pm 0.2$	$5.6 \pm 1.1^a$
2b	$^{12}\text{CO } v = 1-2$ (10 lines)	$-9 \pm 2$	$640^{+220}_{-130}$	...	$0.04 \pm 0.01$
3	$^{13}\text{CO } v = 0-1$ (15 lines)	$-28 \pm 3$	$200 \pm 10$	$1.1 \pm 0.3$	$6.6 \pm 1.8^a$
4	$^{12}\text{CO } v = 0-1$ (24 lines)	$\approx -2$ to $-130$	500 and less		

<sup>a</sup> To obtain  $^{12}\text{CO}$  column densities from  $^{13}\text{CO}$  column densities, the ratio  $^{12}\text{CO}/^{13}\text{CO} = 60$  is used.

emitting gas does not fill the beam uniformly and is clumpy. The clump within which GL 2591 is embedded may well have a motion of several  $\text{km s}^{-1}$  relative to other clumps in the beam. An alternative physical picture which may explain the velocity discrepancy is that the line of sight to GL 2591 looks into a cavity excavated in the process of formation of the large scale bipolar flow. The gas we see may have been accelerated by several  $\text{km s}^{-1}$  relative to the mean velocity of the ambient cloud.

Using the relation  $N(^{13}\text{CO}) = 2 \times 10^{15} A_V \text{ cm}^{-2}$  given by Thronson, Lada, and Hewagama (1985), our  $N_{\text{cold}}(^{13}\text{CO}) = (1.2 \pm 0.2) \times 10^{17} \text{ cm}^{-2}$  implies a visual extinction to GL 2591 of  $A_V = 60$  mag. From near-infrared photometry, Lada *et al.* (1984) have estimated an upper limit to  $A_V$  of about 50 mag. Another estimate of  $A_V$  can be obtained from the optical depth in the silicate feature at  $9.7 \mu\text{m}$ . Using Rieke and Lebofsky's (1985) relation,  $A_V \approx 16.6\tau_{\text{Si}}$ , and the measured optical depth of  $\tau_{\text{Si}} = 4.14$  from Willner *et al.* (1982), we find  $A_V \approx 69$  mag. Our column density of cold  $^{13}\text{CO}$  gas is, therefore, in good agreement with the observed extinction to GL 2591.

Warm CO has been found at the same velocity as the cold molecular cloud gas toward three other infrared sources, viz. S106 IRS 4 (Harris *et al.* 1987), M17 (Harris *et al.* 1987), and W33 A (Mitchell, Allen, and Maillard 1988). The heat source for the warm (or hot) gas is an interesting problem. For the M17 and S106 IRS 4 gas, Harris *et al.* propose heating by ultraviolet radiation from nearby hot stars, via the photoelectric effect on grains. For GL 2591, we favor a model in which the hot gas is thermally coupled to grains heated by the central source. Near-infrared photometry of GL 2591 is well fitted by a compact dust shell with  $T \approx 800 \text{ K}$  (Lada *et al.* 1984). The hot CO we see may well be associated with this dust shell. It is very likely, in fact, that the hot CO is mixed with the hot dust. The spatial distribution of the hot material is of great interest. Unfortunately, the existing data cannot distinguish between a spherical shell and a flattened disk. The observed  $^{13}\text{CO}$  line widths of  $\sim 12 \text{ km s}^{-1}$  are too small to originate in the inner parts of a thin Keplerian disk seen edge-on, but are consistent with the outer cooler regions of a disk, or with a disk seen nearly face-on.

The high-velocity gas, seen in  $^{12}\text{CO}$ , contains temperatures as high as 500 K. It is attractive to interpret this gas as a neutral wind originating at the shell or disk which we see as  $\sim 1000 \text{ K}$  gas with the source velocity. If we assume that the gas and dust are thermally coupled and that the dust is heated by radiation from GL 2591, we can use the relation between dust temperature and distance of Scoville and Kwan (1976) to estimate the distance of the hot gas from GL 2591. We find that the 500 K gas resides at a distance of  $\sim 100 \text{ AU}$  from the source. It has been recognized for some time that the momentum of ionized winds or optical jets is inadequate to drive the extended bipolar gas flows (e.g., Lada 1985). There is no evidence for an ionized wind from GL 2591. The neutral wind we

see in  $^{12}\text{CO}$  is very likely the driver of the extended bipolar flow. At this time, a comparison between the wind momentum and the momentum of the extended bipolar flow is not possible because the bipolar flow has not been mapped in  $^{13}\text{CO}$ . Lizano *et al.* (1988) have detected a neutral wind, of unusual properties, in the bipolar flow source HH 7–11. They find emission from H I with velocities up to  $\sim 170 \text{ km s}^{-1}$  and emission from CO with velocities up to  $\sim 160 \text{ km s}^{-1}$ . They suggest, as one possible explanation, that the atomic hydrogen and the CO coexist in a neutral wind originating from the surface of an embedded protostar. It is most unlikely that the neutral outflow from GL 2591 can begin at the surface of the embedded object because GL 2591 is a luminous object with, almost certainly, a high effective temperature. The existence of neutral outflows from both low-luminosity and high-luminosity young stellar objects (YSOs) is intriguing and may imply a common mechanism.

It is not clear where the CO feature at  $-28 \text{ km s}^{-1}$  fits into the picture of GL 2591. The column density of the  $-28 \text{ km s}^{-1}$  feature is high,  $N(^{12}\text{CO}) \approx 7 \times 10^{18} \text{ cm}^{-2}$  if  $^{12}\text{CO}/^{13}\text{CO} = 60$ . Because it is warm ( $T \approx 200 \text{ K}$ ), the gas is probably close to the central object. If we assume gas heating by collision with grains, the distance of the 200 K gas from GL 2591 is  $\sim 1000 \text{ AU}$  (again using Scoville and Kwan 1976). In a spectrum of the infrared source GL 490, we found an absorption feature blueshifted by  $16 \text{ km s}^{-1}$  relative to the central source (Mitchell *et al.* 1988a). In that case, although we had no temperature information, we suggested that the feature was due to a recently ejected shell or fragment. For both GL 2591 and GL 490, the blueshifted feature is not seen in CO radio emission spectra, suggesting that the gas does not fill the radio beam. The cold, high-velocity CO seen in emission may have a clumpy distribution: Plambeck, Snell, and Loren (1983) deduce, from a sample of 10 outflow sources, a beam filling factor of  $\sim 0.15$ . Canto, Rodriguez, and Anglad (1987) have pointed out, however, that the CO observations do not imply a small beam-filling factor if a temperature gradient is present. Even if clumping is not general, gas fragments are seen near low-mass YSOs (as Herbig-Haro objects) and may well exist near the more heavily obscured massive YSOs. If the clumps are ejected from the central object, as in the "interstellar bullet" model of Norman and Silk (1979), the  $-28 \text{ km s}^{-1}$  feature toward GL 2591 may be one such clump. Under the simplest assumption of no acceleration, the time taken from the clump (or shell) to travel 1000 AU is  $\sim 240 \text{ yr}$ . Reobservation of GL 2591 (and other sources, such as M8E-IR (Mitchell *et al.* 1988b) and GL 490) on a fairly short time scale might well reveal changes with time.

We thank the staff of the CFHT for its support. This work was supported by an operating grant from the Natural Sciences and Engineering Research Council of Canada (to G. F. M.).

#### REFERENCES

- Bally, J., and Lada, C. J. 1983, *Ap. J.*, **265**, 824.  
 Campbell, B. 1984, *Ap. J.*, **287**, 334.  
 Canto, J., Rodriguez, L. F., and Anglada, G. 1987, *Ap. J.*, **321**, 877.  
 Carroll, T. J., and Goldsmith, P. F. 1981, *Ap. J.*, **245**, 891.  
 Forrest, W. J., and Shure, M. A. 1986, *Ap. J. (Letters)*, **311**, L81.  
 Geballe, T. R., and Wade, R. 1985, *Ap. J. (Letters)*, **291**, L55.  
 Harris, A. I., Stutzki, J., Genzel, R., Lugten, J. B., Stacey, G. J., and Jaffey, D. T. 1987, *Ap. J. (Letters)*, **322**, L49.  
 Kirby-Docken, K., and Liu, B. 1978, *Ap. J. Suppl.*, **36**, 359.  
 Lacy, J. H., Baas, F., Allamandola, L. J., Persson, S. E., McGregor, P. J., Lonsdale, C. J., Geballe, T. R., and van de Bult, C. E. P. 1984, *Ap. J.*, **276**, 533.

- Lada, C. 1985, *Ann. Rev. Astr. Ap.*, **23**, 267.  
 Lada, C. J., Thronson, H. A., Jr., Smith, H. A., Schwartz, P. R., and Glaccum, W. 1984, *Ap. J.*, **286**, 302.  
 Lizano, S., Heiles, C., Rodriguez, L. F., Koo, B.-C., Shu, F. H., Hasegawa, T., Hayashi, S., and Mirabel, I. F. 1988, *Ap. J.*, **328**, 763.  
 Maillard, J.-P., and Michel, G. 1982, in *IAU Colloquium 67, Instrumentation for Astronomy with Large Optical Telescopes*, ed. C. M. Humphries (Dordrecht: Reidel), p. 213.  
 McKee, C. F., Storey, J. W. V., Watson, D. M., and Green, S. 1982, *Ap. J.*, **259**, 647.  
 Mitchell, G. F., Allen, M., and Maillard, J.-P. 1988, *Ap. J. (Letters)*, **33**, L55.  
 Mitchell, G. F., Allen, M., Beer, R., Dekany, R., Huntress, W., and Maillard, J.-P. 1988a, *Astr. Ap.*, **201**, L16.  
 ———. 1988b, *Ap. J. (Letters)*, **327**, L17.  
 Mozurkewich, D., Schwartz, P. R., and Smith, H. A. 1986, *Ap. J.*, **311**, 371.  
 Norman, C., and Silk, J. 1979, *Ap. J.*, **228**, 197.  
 Plambeck, R. L., Snell, R. L., and Loren, R. B. 1983, *Ap. J.*, **266**, 321.  
 Rieke, G. H., and Lebofsky, M. J. 1985, *Ap. J.*, **288**, 618.  
 Schonberg, K. 1988, *Astr. Ap.*, **195**, 198.  
 Scoville, N. Z., and Kwan, J. 1976, *Ap. J.*, **206**, 718.  
 Scoville, N. Z., Hall, D. N. B., Kleinmann, S. G., and Ridgway, S. T. 1983, *Ap. J.*, **275**, 201.  
 Spitzer, L., Jr. 1978, *Physical Processes in the Interstellar Medium* (New York: Wiley).  
 Storey, J. W. V., Watson, D. M., Townes, C. H., Haller, E. E., and Hansen, W. L. 1981, *Ap. J.*, **247**, 136.  
 Thompson, R. I., and Tokunaga, A. T. 1979, *Ap. J.*, **231**, 736.  
 Thronson, H. A., Lada, C. J., and Hewagama, T. 1985, *Ap. J.*, **297**, 662.  
 Viscuso, P. J., and Chernoff, D. F. 1988, *Ap. J.*, **327**, 364.  
 Wannier, P. G. 1980, *Ann. Rev. Astr. Ap.*, **18**, 399.  
 Willner, S. P., et al. 1982, *Ap. J.*, **253**, 174.  
 Yamashita, T., et al. 1987, *Pub. Astr. Soc. Japan*, **39**, 809.

MARK ALLEN: Earth and Space Sciences Division, Jet Propulsion Laboratory, 4800 Oak Grove Drive, Pasadena, CA 91109

CHARLES CURRY and GEORGE F. MITCHELL: Department of Astronomy, Saint Mary's University, Halifax, N. S., B3H 3C3, Canada

JEAN-PIERRE MAILLARD: Institut d'Astrophysique, boulevard Arago, F-75014 Paris, France